SAND REPORT

SAND2002-1906
Unlimited Release
Printed June 2002

Small-Scale High-Performance Optics

Christopher W. Wilson, Barry L. Spletzer, Chris L. Leger

Prepared by
Sandia National Laboratories
Albuquerque, New Mexico 87185 and Livermore, California 94550

Sandia is a multiprogram laboratory operated by Sandia Corporation,
a Lockheed Martin Company, for the United States Department of
Energy under Contract DE-AC04-94AL85000.

Sandia National Laboratories

Issued by Sandia National Laboratories, operated for the United States Department of Energy by Sandia Corporation.

Available to DOE and DOE contractors from
U.S. Department of Energy
Office of Scientific and Technical Information
P.O. Box 62
Oak Ridge, TN 37831

Telephone: (865)576-8401
Facsimile: (865)576-5728
E-Mail: reports@adonis.osti.gov
Online ordering: http://www.doe.gov/bridge

Available to the public from
U.S. Department of Commerce
National Technical Information Service
5285 Port Royal Rd
Springfield, VA 22161

Telephone: (800)553-6847
Facsimile: (703)605-6900
E-Mail: orders@ntis.fedworld.gov
Online order: http://www.ntis.gov/ordering.htm

SAND2002-1906
Unlimited Release
Printed June 2002

Small–Scale High-Performance Optics

Christopher W. Wilson and Chris L. Leger
Intelligent Systems Sensors

Barry L. Spletzer
Intelligent Systems Controls

Sandia National Laboratories
P.O. Box 5800
Albuquerque, NM 87185-1003

Abstract

Historically, high resolution, high slew rate optics have been heavy, bulky, and expensive. Recent advances in MEMS (Micro Eloctro Mechanical Systems) technology and micro-machining may change this. Specifically, the advent of steerable sub-millimeter sized mirror arrays could provide the breakthrough technology for producing very small-scale high-performance optical systems. For example, an array of steerable MEMS mirrors could be the building blocks for a Fresnel mirror of controllable focal length and direction of view. When coupled with a convex parabolic mirror the steerable array could realize a micro-scale pan, tilt and zoom system that provides full CCD sensor resolution over the desired field of view with no moving parts (other than MEMS elements).

This LDRD provided the first steps towards the goal of a new class of small-scale high-performance optics based on MEMS technology. A large-scale, proof of concept system was built to demonstrate the effectiveness of an optical configuration applicable to producing a small-scale (< 1cm) pan and tilt imaging system. This configuration consists of a color CCD imager with a narrow field of view lens, a steerable flat mirror, and a convex parabolic mirror. The steerable flat mirror directs the camera's narrow field of view to small areas of the convex mirror providing much higher pixel density in the region of interest than is possible with a full 360 deg. imaging system. Improved image correction (dewarping) software based on texture mapping images to geometric solids was developed. This approach takes advantage of modern graphics hardware and provides a great deal of flexibility for correcting images from various mirror shapes. An analytical evaluation of blur spot size and axi-symmetric reflector optimization were performed to address depth of focus issues that occurred in the proof of concept system. The resulting equations will provide the tools for developing future system designs.

Acknowledgements

The author would like to acknowledge the contributions of Eric Gottlieb and Dan Small for their assistance with the texture mapping algorithms; Bill Sweatt for his expert optical support and guidance, Mial Warren and Tom Zipirian for their encouragement and support; and Sid Gutierrez for his programmatic guidance and support.

Contents

Figures

Tables

Introduction

The application of micro-scale technologies to the realization of high-performance optical imaging systems is a new field. To achieve the full potential of such devices requires the development of new MEMS structures, optical configurations, and control and image manipulation techniques. As a first step towards reaching this goal we proposed to implement a new optical configuration with potential for small-scale application at a large-scale proof of concept level. This allowed us to develop some of the image control and image correction techniques that will be required for small-scale implementation. In parallel, we investigated resolution limitations for various mirror geometries based on blur spot analysis and developed optimization tools for mirror design.

This work focusses on demonstrating the feasibility of a new optical configuration applicable to a MEMS scale high-performance imaging system. The potential payoff for this research is huge as we apply these micro-scale technologies to high-performance optics to produce high-quality, high-resolution imaging devices in unprecedented small scale. In addition to their extremely small size, these devices should be very fast, consume little power and be inexpensive. Applications include miniature inspection probes for manufacturing or medicine, imaging systems for small-scale robot control and navigation, and low observable surveillance or monitoring systems. Other new and unforeseen applications using small-scale high-performance low-cost optical systems based on this technology will no doubt arise as the research expands. The Navy, Air Force, and DARPA are potential customers for this technology.

Conceptual Designs

An extremely compact pan, tilt and zoom imaging optical system is one application that might benefit from the application of MEMS technologies. We have generated several conceptual designs of potential optical configurations that could be constructed on a MEMS scale.

The proposed optical geometries are derived from a type of 360-degree camera system that has been investigated for many years [1] and is currently available from several sources. Figure 1. shows the basic optical geometry and an outline of the raw image produced by the video camera. This donut shaped image can be dewarped such that the annulus of valid image data produces a correctly proportioned rectangular image covering 360 degrees left to right and 90 to 120 degrees top to bottom. Note that the annulus represents a subset of the pixels in the original image (the corners and center of the image are not used). This indicates that the full field of view is represented at a significantly reduced resolution compared to what would be expected if the camera with a limited field of view were pointed directly at a portion of the scene. Conceptually, each of the following optical systems achieves high resolution by applying more image pixels to a smaller region of the parabolic mirror.

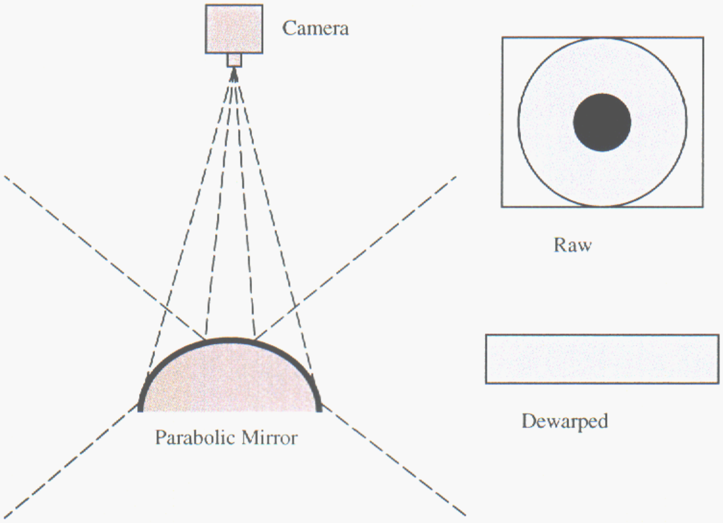

Figure 1. 360-Degree Camera and Images

A sketch of the MEMS based high-performance pan, tilt and zoom optical system is shown in Figure 2. We believe this configuration could be built in a volume <1 cc. The high density, large element count, steerable MEMS mirror array does not currently exist and the control scheme for producing desired pan, tilt, zoom and focus have not been developed. This system will require a significant development effort.

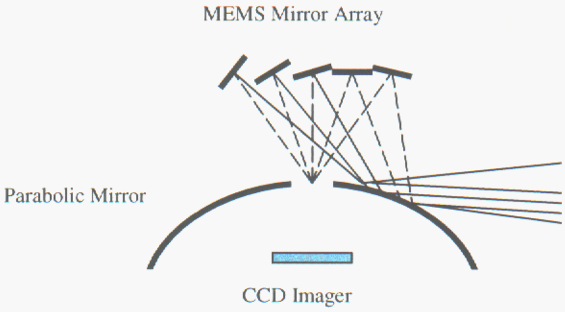

Figure 2. MEMS Pan, Tilt and Zoom

A simpler single MEMS mirror system providing full 360-degree field of view plus a steerable high resolution 'fovea' is shown in Figure 3. A single steerable mirror with a dimension of 1 to 2 mm has been fabricated here at Sandia National Laboratories and could be directly applicable to such a system. This system produces the same raw image as the 360-degree camera except that the center of the annulus is directed towards a small section of the full field of view.

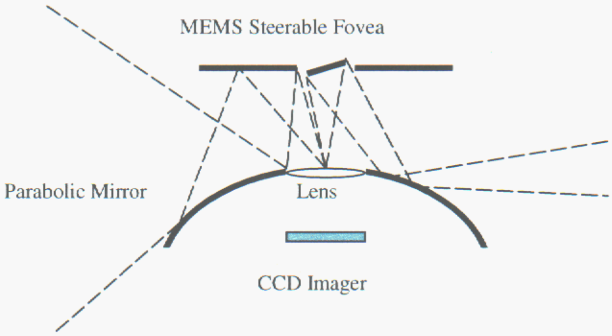

Figure 3. MEMS Steerable Fovea

Proof of Concept System

A sketch of the proof of concept system developed under this LDRD is shown in Figure 4. The camera from a 360-degree camera system (Figure 1) is separated from the parabolic mirror and moved to the side and a single steerable flat mirror is inserted in the optical path. The steerable mirror applies all of the image pixels to a small area on the parabola. The proof of concept system allowed us to develop the image correction algorithms needed to map the CCD image through the steerable flat mirror and the parabolic mirror into the world.

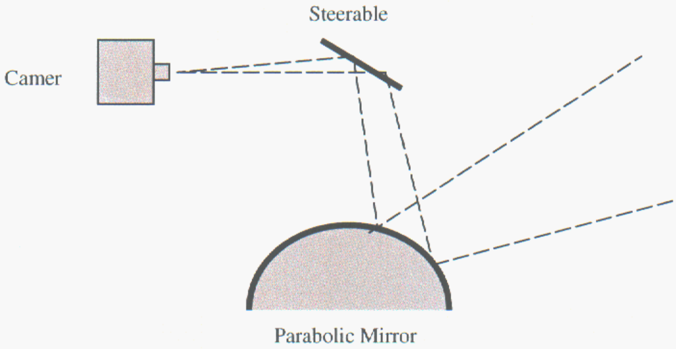

Figure 4. Proof of Concept

The hardware used in the proof of concept system is listed in Table 1. This system was constructed from existing components at relatively low cost. Figures 5 and 6 show the video camera and lens, the flat steerable mirror, and the convex parabolic mirror from top and side views respectively. Note that optical axis of the lens and the axis of parabolic mirror lie in a horizontal plane in the proof of concept system. This allows the gimbal mounted mirror to behave in a tip-tilt mode similar to the MEMS mirror components under development rather than in a pan–tilt mode.

	Hardware Components
1	Sentec ST630 1/3" CCD color camera
2	Computar 50mm f1.4 C-mount Lens
3	C-mount extension tube set (20mm-25mm)
4	Imagenation PXC 200 color frame grabber
5	Directed Perception PTU-46-70G Gimbal Pan and Tilt
6	Dell Dimension 4100 1GHz computer
7	NVIDIA GeForce 2 graphics card
8	2" x 2" front surface mirror
9	1.5” D x 1.0” H parabolic mirror

Table 1. Hardware Components Proof of Concept System

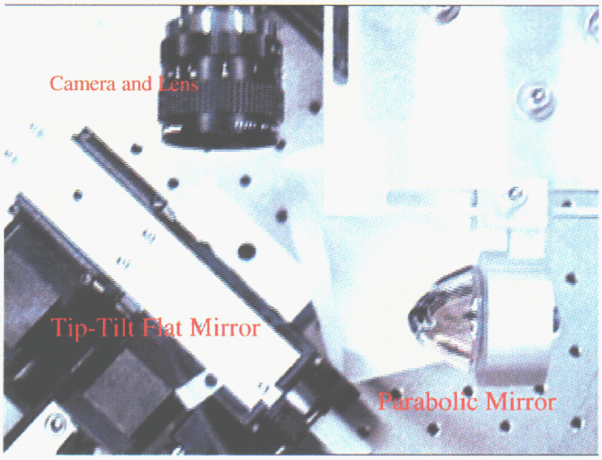

Figure 5. Proof of Concept System Top View

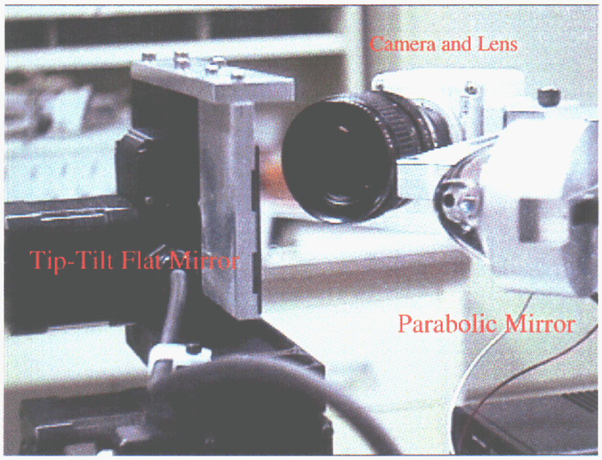

Figure 6. Proof of Concept System Side View

The proof of concept system generates images that cover roughly 1/4 of the parabolic mirror diameter (1/4 the original field of view). This translates into a 16 to 1 increase in pixel density compared to the full 360 deg. field of view. Figures 7 shows the raw image from a full mirror diameter field of view. Figure 8 shows ¼ mirror diameter field of view images from a) the proof of concept system and b) an enlargement of the same region in Figure 7. The increased resolution produced by the proof of concept system is readily apparent. The word “CAUTION” is clearly visible in Figure 8a) as is the needle position in the pressure guage while neither can be decerned in Figure 8b).

It is also apparent in Figure 8a that only part of the image is in focus. The scene presented to the camera by the convex mirror exists slightly within the mirror’s surface (see section on Blur Spot

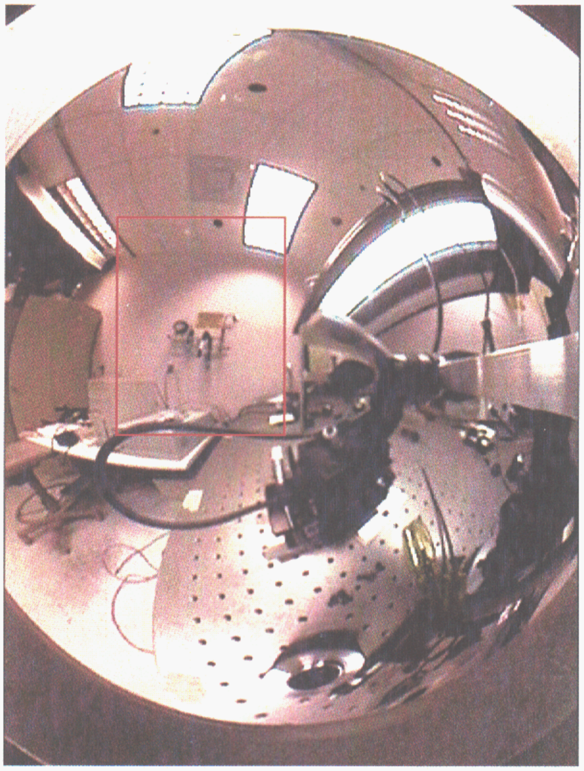

Figure 7: Conventional 360 deg Image

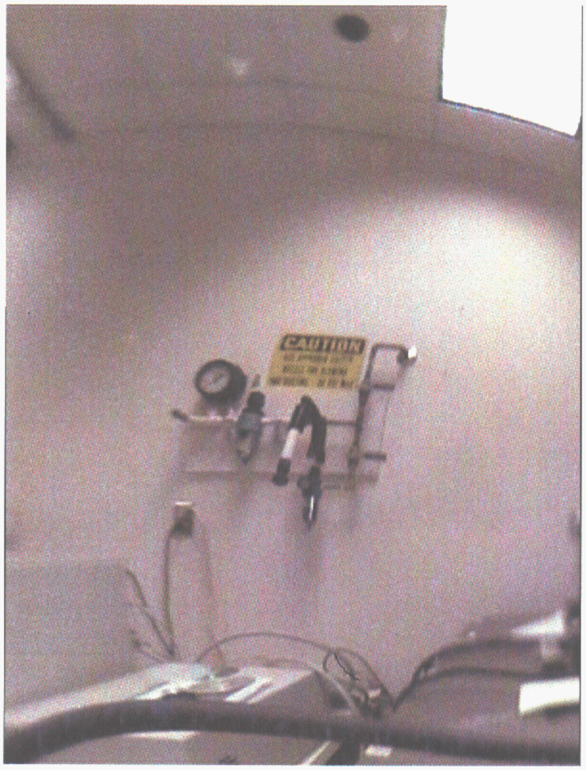

Figure 8a: Concept System Image

Figure 8b: Conventional 360 deg Zoom

Analysis and Axisymmetric Reflector Optimization). The standard C-mount lens used in the concept system required 20 to 25 mm of extension tubes to focus on the image in the convex mirror. The depth of focus at maximum aperture (f1.4) was only a few mm and even at f8 was not sufficient to focus all the way across the field of view. As the field of view moved from the edge of the mirror to the center, the distance from the camera to the mirror surface changed by approximately 25mm. Inorder to maintain focus in the area of interest, the lens had to be repeatedly refocused as the field of view moved across the convex mirror surface. This depth of focus issue lead to the blur spot analysis and convex mirror optimization presented later in this report. An auto-focusing lens and more sensitive camera (smaller aperture) would reduce the impact of the depth of focus limitations experienced with the proof of concept system. We also contacted a lens manufacturer [2] that claims to have a lens that focuses from 1/4 in. to infinity. We were unable to obtain a lens to test during this project. An optimized parafocal reflector would provide a true solution.

Image Correction Software

During a previous project, one of the authors (Chris Leger) had developed software to map a 360 deg. image onto a rectangle using a lookup table. This lookup table converted the radial location of a pixel in the 360 deg. image into the vertical axis of the rectangular image and the angular location in the 360 deg. image into the horizontal axis. This produced a geometrically correct image but the resulting image was very granular.

For this project we implemented new image correction software based on computer graphics texture mapping techniques. Texture mapping refers to the computer graphics technique of mapping a texture (an image) onto a graphics geometry. The vertices of a geometric shape are mapped into image coordinates, that is each vertex is assigned an image coordinate. As the geometry is rendered, the image is warpped such that the image coordinate associated with a given vertex remains attached to that vertex and the image appears attached to the geometric surface. Figure 9 shows a triangulated parabolic surface, the underlying geometry. Figure 10 shows the raw image texture mapped onto the parabolic surface. Since the vertex is associated with an image coordinate rather than an image value (color or intensity), the image can be updated (live video) and the updated image will appear on the geometric surface. This mapping, image warping, and rendering is acomplished by modern graphics hardware requiring little overhead of the host CPU. We applied the 360 deg. raw image (Figure 11) to several shapes including a rectangular plate (Figure 12), the inside of a cylinder (Figure 13), and the exterior and interior of a sphere. Once the mapping is defined, the operator can manipulate the geometric object on the computer screen to view different parts on the image. One of the most effective mappings was to the interior of a sphere. By fixing the view point at the center of the sphere, the operator was provided with a window onto the world imaged by the 360 deg camera. Panning and tilting the window around the world was very fast and intuitive [3]. The texture mapping algorithms developed for this project were implemented using Sandia’s Umbra software architecture [4].

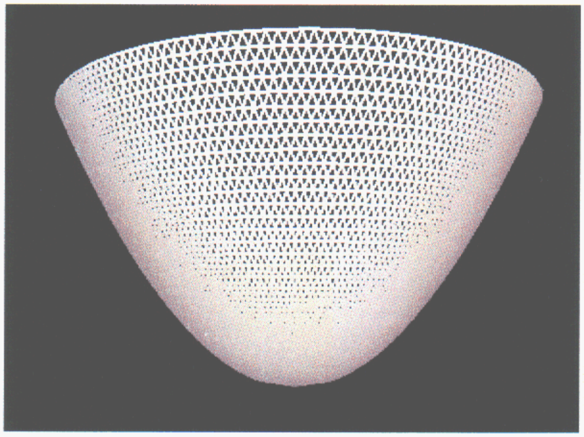

Figure 9: Triangulated Parabolic Surface

Figure 10: Parabolic Surface Texture Map

A program to correct high resolution images from a sub-section of the parabolic reflector was also developed. Our initial implementation approximated the imaging geometry with a rectangular sub-section of the full parabolic mirror image. While this mapping is not exactly correct it provided a very adequate correction for viewing.

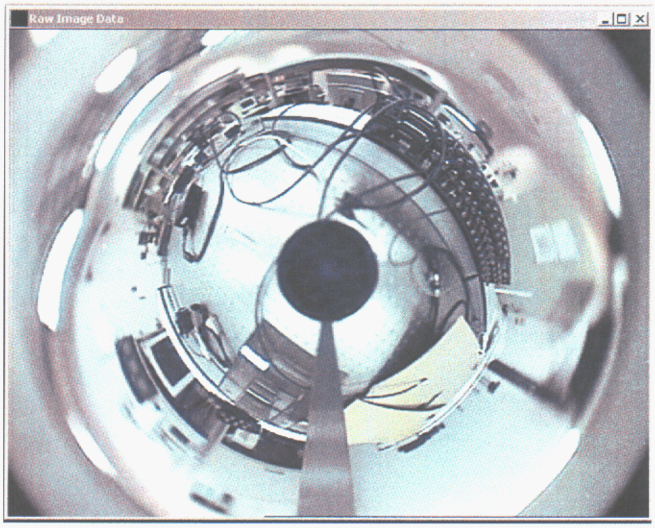

Figure 11: Raw Image of Full Mirror

Figure 12: Image Texture Mapped to Planar Rectangular Surface

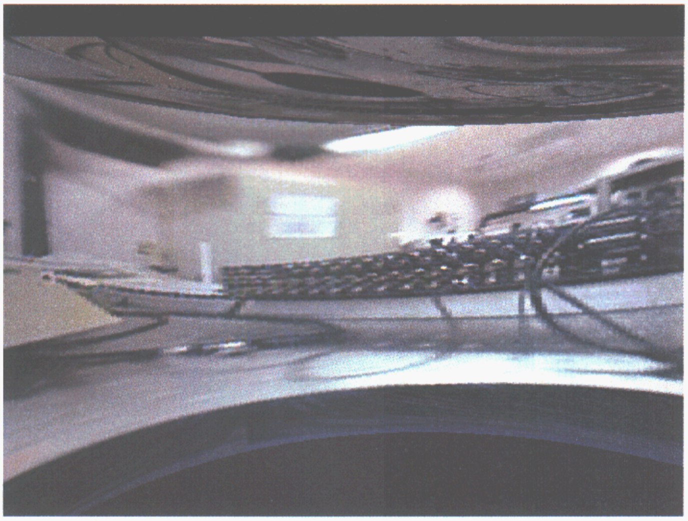

Figure 13: Image Texture Mapped to Interior of a Cylinder

Blur Spot Analysis and Axi-symmetric Reflector Optimization

The use of a convex mirror to provide a 360 degree field view lens is not new. Such systems are commercially available. Normally the shape of the convex mirror is that of a paraboloid or hyperboloid. The specific shape is chosen to simplify the dewarping algorithms required to convert the donut shaped raw image into a rectangular panoramic picture. The advent of high-speed computing and, in particular, advanced graphics display devices has made this conversion process much simpler. Now, even relatively complex dewarping algorithms can be implemented in real-time with relatively modest hardware. This allows other convex mirror shapes to be investigated that could have the potential to optimize other aspects of the system performance. This section examines some of these potential optimization avenues and presents useful relationships that could be used to design an axisymmetric reflector with minimized blur spot, minimized astigmatism, or parafocal performance.

Preliminary Relationships

Begin the analysis by examining the behavior of an incoming light ray striking the mirror and being reflected so it passes through the center of the aperture of a camera lens and onto the lens focal plane. For now, the characteristics of the lens and focal plane are not of interest. The analysis of this general ray will be used extensively to derive the overall properties of the mirror.

Figure 14 shows a schematic of this ray and its interaction with the mirror and the aperture. In the figure, the incoming ray enters at a colatitude (measured clockwise from the positive z-axis) of ϕ and strikes the mirror at location (r_m, z_m) with surface unit normal **n**. The ray reflects, leaving the mirror at colatitude ϕ_r and passing through the pinhole and on to the focal plane. The equal angles of incidence and reflection are labelled α in the figure. The coordinate system is defined with the origin at the center of the aperture (here the pinhole), and the z-axis along the axis of symmetry of the system. The x-axis is aligned with the incoming ray. Now consider the geometric relationships that can be derived from this arrangement.

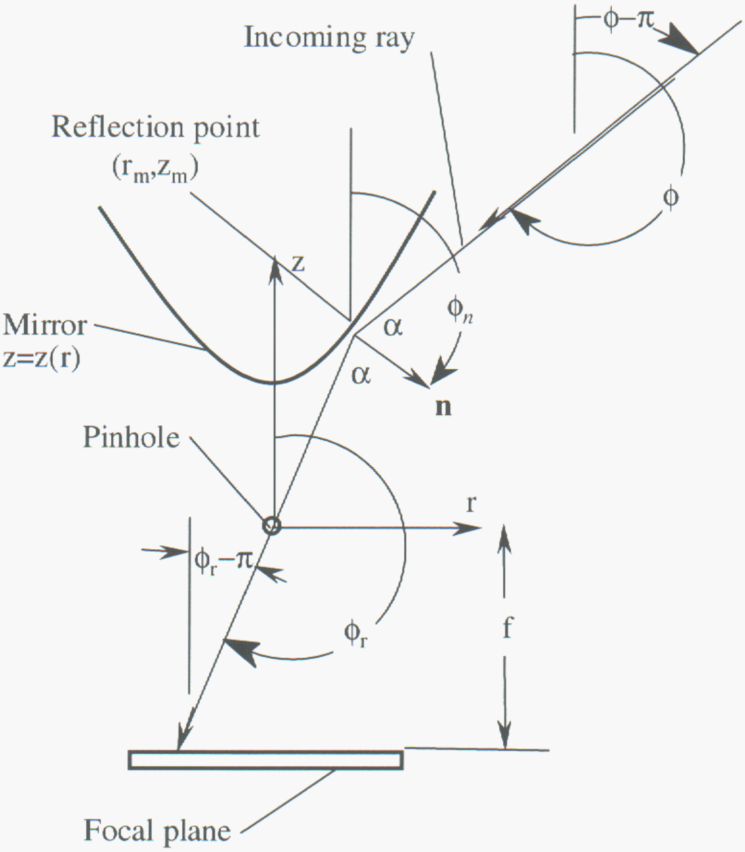

Figure 14: Schematic of a reflected ray passing through the origin

Calling the colatitude of the surface normal ϕ_n:

$$\phi_n = \phi - \pi + \alpha \qquad\qquad \phi_n + \alpha = \phi_r \tag{1}$$

So:

$$\phi_r = 2\phi_n - \phi + \pi \tag{2}$$

The location of the reflection point is related to the reflected angle by:

$$\rho = \frac{r_m}{z_m} = \tan(\phi_r - \pi) = \tan(2\phi_n - \phi) \tag{3}$$

Where ρ is defined here as a convenient dimensionless parameter. The slope of the mirror at the reflection point is the derivative of the mirror surface function with respect to *r*:

$$z' = \left.\frac{dz}{dr}\right|_{r=r_m} = \tan(\pi - \phi_n) \tag{4}$$

And combining these relationships, the various angles of interest can be related directly as functions of ρ and z':

$$\begin{gathered} \phi_n = \pi - \operatorname{atan} z' \qquad \phi_r = \pi + \operatorname{atan} \rho \qquad 2\phi_n - \phi = \operatorname{atan} \rho \\ \phi = 2\phi_n - \phi_r + \pi = -2\operatorname{atan} z' - \operatorname{atan} \rho \end{gathered} \tag{5}$$

The manipulation of these angles requires a number of trigonometric identities. Since some of them are not well known, they are included here:

$$
\begin{aligned}
&\cos 2x = 2\cos^2 x - 1 \quad 1 - \cos 2x = 2\sin^2 x \\
&\cos(\operatorname{atan} x) = \frac{1}{\sqrt{1+x^2}} \quad \sin(\operatorname{atan} x) = \frac{x}{\sqrt{1+x^2}} \\
&\tan(2\operatorname{atan} x + \operatorname{atan} y) = y - 2x\frac{1+y^2}{x^2+2xy-1} \\
&\sin(2\operatorname{atan} x + \operatorname{atan} y) = \frac{1}{\sqrt{1+y^2}}\left[\frac{2(x+y)}{1+x^2} - y\right]
\end{aligned}
\tag{6}
$$

Applying these identities to the parameters of interest yields:

$$
\begin{aligned}
&\sin(2\phi_n - \phi) = \frac{\rho}{\sqrt{1+\rho^2}} && \cos(2\phi_n - \phi) = \frac{1}{\sqrt{1+\rho^2}} \\
&\sin\phi = \frac{-1}{\sqrt{1+\rho^2}}\left[\frac{2(\rho+z')}{1+z'^2} - \rho\right] && \tan\phi = 2z'\frac{1+\rho^2}{z'^2+2z'\rho-1} - \rho \\
&\sin 2\phi_n = \frac{-2z'}{1+z'^2} && \cos 2\phi_n = \frac{1-z'^2}{1+z'^2}
\end{aligned}
\tag{7}
$$

The direction of the reflected ray, based on the incoming ray and the properties of the reflection point, can be determined by using the following relation between the incident beam vector (**I**) the reflected beam vector (**R**) and the local mirror normal vector (**n**):

$$
\mathbf{R} = \mathbf{I} - 2\mathbf{n}(\mathbf{n}\cdot\mathbf{I}) \tag{8}
$$

Aligning the coordinate system so the incoming ray is parallel to the x-z plane gives the incoming ray and surface normal the following forms:

$$
\mathbf{I} = \begin{bmatrix} \sin\phi \\ 0 \\ \cos\phi \end{bmatrix} \qquad \mathbf{n} = \begin{bmatrix} \sin\phi_n \cos\theta \\ \sin\phi_n \sin\theta \\ \cos\phi_n \end{bmatrix} \tag{9}
$$

Where θ is the azimuth of the reflection point measured from the positive *x*-axis. Applying Equation 8 to these vectors:

$$\mathbf{R} = -\begin{bmatrix} \left[(1-\cos 2\phi_n)\cos\theta\sin\phi + \sin 2\phi_n \cos\phi\right]\cos\theta - \sin\phi \\ \left[(1-\cos 2\phi_n)\cos\theta\sin\phi + \sin 2\phi_n \cos\phi\right]\sin\theta \\ \sin 2\phi_n \cos\theta\sin\phi + \cos 2\phi_n \cos\phi \end{bmatrix} \tag{10}$$

This is the general direction of a reflected ray. This relation is central to the analysis of the mirror.

Azimuthal Blur Spot Size

One crucial issue in determining the performance of an axisymmetric mirror is the resolution or clarity of the image formed. The optical system discussed here is a little unusual in that the axisymmetric reflector is placed between a camera lens and the object to be imaged. In order for a camera lens to image an object clearly, the light rays from the point to be imaged must be parallel or diverging as from a point source. Ordinarily light from an object does behave this way. However, here the mirror changes the path of the incoming light. This section will assess how the light path is changed and what effect this has on the image formed.

One way to assess the resolution of a system is to examine the blur spot size. This is usually defined as the area on the focal plane that contains all the light rays emanating from a point source. Because we're interested specifically in the axisymmetric reflector and not the specifics of a camera lens, here the blur spot will be defined slightly differently. Figure 15 shows a number of parallel rays reflecting from a curved mirror and passing through a camera aperture. The incoming bundle of parallel rays represents the light from a distant point.

If the rays through the aperture are traced backwards in a straight line (see the extended rays in the figure), they will not generally all intersect at the same point. If they did, then the reflected rays could be imaged the same as if they originated from a real object. Instead, there is a minimum ray bundle size that limits the resolution. One way to express this is to calculate the ratio of the minimum bundle size to its distance from the camera aperture. This is the angular size of the blur spot which then can be used directly along with the focal length of the lens to determine the size of the blur spot in the focal plane. What follows here are some relationships derived to estimate the size of this blur spot.

Although it may not be obvious from Figure 15, as the aperture become smaller the minimum bundle size is also reduced. First consider where the extended rays from a reflected parallel bundle will intersect for a very small aperture. Equation 10 gives the generally equation for a reflected ray. The y coordinate of the reflection point for a ray striking the mirror surface at an azimuth angle of θ is:

$$y_m = r_m \sin\theta \tag{11}$$

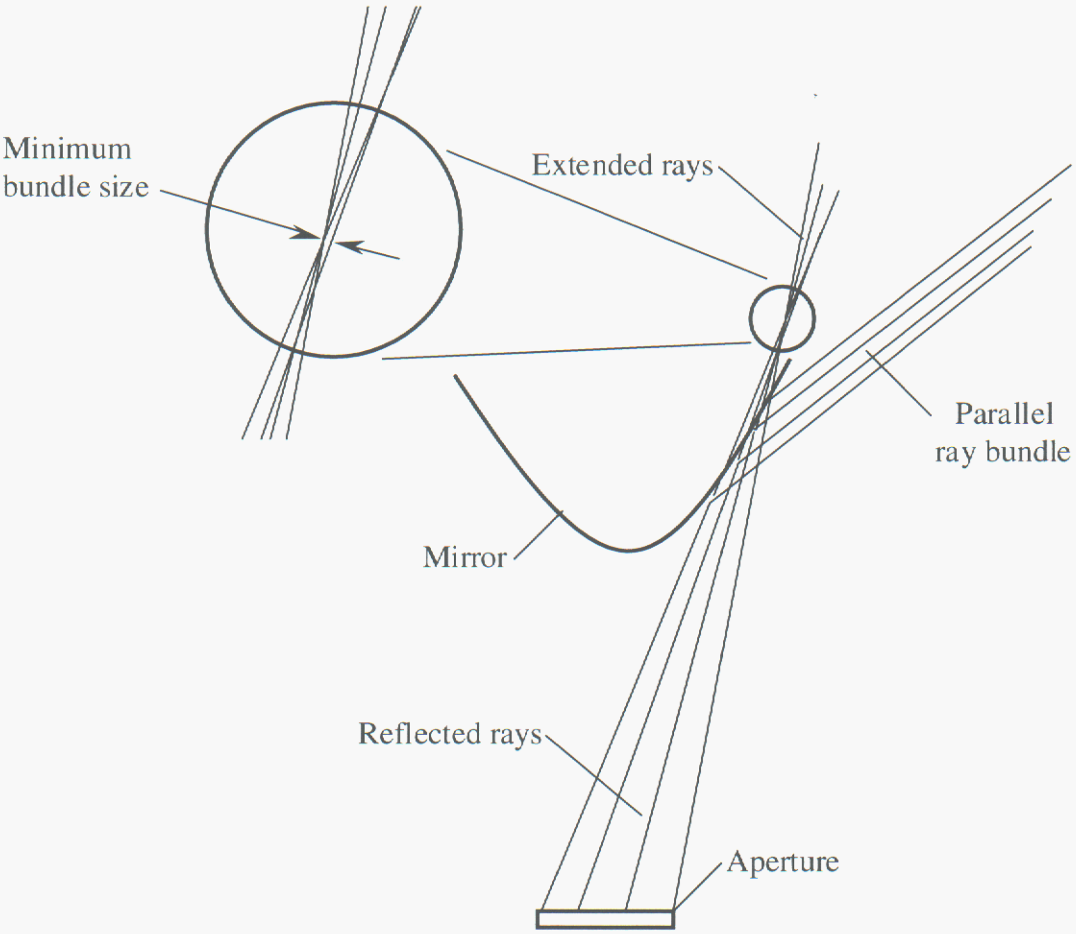

Figure 15: Minimum ray bundle of an axisymmetric reflector

by using the direction of the reflected ray a relationship between the *y* and *z* coordinates of the extended ray can be derived:

$$y = y_m + \frac{dy}{dz}(z - z_m) = r_m \sin\theta + \frac{\mathbf{R_y}}{\mathbf{R_z}}(z - z_m) \tag{12}$$

Where $\mathbf{R_y}$ and $\mathbf{R_z}$ are the components of the **R** vector of Equation 10. The rays incident at $+\theta$ and $-\theta$ will intersect at *y=0*. For small values of θ, determine the *z* coordinate of this intersection. This value will be called the focal point of the mirror. Rays reflecting off the mirror at a constant z_m will appear to emanate from this location. Setting *y* to zero, substituting the values for the reflected ray direction, and solving for *z*:

$$z = z_m - \frac{\sin 2\phi_n \cos\theta \sin\phi + \cos 2\phi_n \cos\phi}{[\cos\theta \sin\phi(1 - \cos 2\phi_n)] + \sin 2\phi_n \cos\phi} r_m \tag{13}$$

For a small aperture, look at this relation as $\theta \to 0$:

$$z_0 = \lim_{\theta \to 0} z = z_m - \frac{\cos(2\phi_n - \phi)}{\sin(2\phi_n - \phi) + \sin\phi} \tag{14}$$

Applying the various trig identities:

$$\frac{z_0}{r_m} = \frac{1}{\rho} + \frac{1}{2} \frac{1 + z'^2}{z'(1 - \rho z')} \tag{15}$$

The point z_0 is the intersection point for rays passing trough the aperture near the center and that have reflection points of constant z. Now look at how the size of the ray bundle increases as rays at greater azimuth (θ) are considered. The halfwidth of the ray bundle is the value of y (Equation 12) at the focal point (z_0).

$$y_f = r_m \sin\theta \left[1 + \frac{\cos\theta \tan\phi(\cos 2\phi_n - 1) - \sin 2\phi_n}{\sin 2\phi_n \cos\theta \tan\phi + \cos 2\phi_n} \frac{z_0 - z_m}{r_m} \right] \tag{16}$$

Substituting the trig identities:

$$\frac{y_f}{r_m} = \sin\theta \left[1 + \frac{\left[2z' - \rho\left(z'^2 - 1\right)\right] z' \cos\theta - \left(z'^2 - 1\right) - 2\rho z'}{2\left[\left[2z' - \rho\left(z'^2 - 1\right)\right] z' \cos\theta + \left(z'^2 - 1\right)\right]\left[z'^2 - 1 + 2\rho z'\right]} \frac{z'^2 + 1}{1 - \rho z'} \right] \tag{17}$$

The parameter y_f is the half width of the ray bundle in the azimuthal direction at the focal point. So far the variation in width of the bundle caused by reflection points up and down the radiant has been ignored. The ray bundle in the meridional direction is dependent on the shape and local curvature of reflector. The relation derived so far is a lower bound for the ray bundle width that is largely independent of mirror shape.

So far, the relationship derived is in terms of the azimuth of the reflection point (θ). This is not a suitable parameter for a system design. Instead it is necessary to relate the azimuth of the reflection point to the aperture size. This is done by noting that the reflected ray that passes through the edge of the aperture along the y-axis at $(0, R, 0)$ and the reflection point at $(r_m\cos\theta, y_m\cos\theta, z_m)$ is the limiting ray for the azimuthal blur spot and has a direction of:

$$\begin{bmatrix} 0 \\ R \\ 0 \end{bmatrix} - \begin{bmatrix} r_m \cos\theta \\ r_m \sin\theta \\ z_m \end{bmatrix} \tag{18}$$

By performing a reflection operation on a ray in this direction results in an incoming ray that produced this ray at the edge of the aperture. By the definition of the coordinate system, the y component of the incoming ray is 0. The relationship between the aperture radius (R) and the azimuthal position corresponding that radius can then be derived. Performing the reflection and setting the y component to zero:

$$0 = \left[1 - \left(1 - \cos 2\phi_n\right)\sin^2\theta\right]R + \left(\frac{z_m}{r_m}\sin 2\phi_n - \cos 2\phi_n\right)r_m \sin\theta \tag{19}$$

Introducing the dimensionless variable for the aperture radius of $\Lambda = R/z_m$, performing the trigonometric substitutions, and solving the resulting quadratic in $\sin\theta$ results in:

$$\sin\theta = \frac{\sqrt{\left[2z' + \left(1 - z'^2\right)\rho\right]^2 + 8\Lambda^2\left(1 + z'^2\right)z'^2} - 2z' - \left(1 - z'^2\right)\rho}{4\Lambda z'^2} \tag{20}$$

Equations 17 and 20 then can be used to determine the blur spot size as a function of the aperture size and mirror shape parameters. The azimuthal halfwidth of the ray bundle has been defined here as the halfwidth at the focal point. The blur spot will be somewhat smaller than that, since it lies between the focal point and the point where the rays from the edge of the aperture intersect. A reasonable approximation for this value is half the total width of the bundle at the focal point. This is the parameter y_f previously determined. Although this is not precisely the size of the spot, it is a suitable measure of the performance of the mirror. The blur spot can be expressed in radians by dividing y_f by the distance from the aperture z_m+z_0. This angular value of the blur spot then can be used directly to determine the blur spot size on the focal plane which is the product of the camera lens focal length and the spot angular size. The angular size of the blur spot is:

$$B = \frac{y_f}{z_m + z_0} = \frac{\dfrac{y_f}{r_m}}{\dfrac{1}{\rho} + \dfrac{z_0}{r_m}} \tag{21}$$

$$B = \frac{\rho z' \sin\theta}{4z' - 3\rho z'^2 + \rho}\left[3 - 2\rho z' + z'^2 - \frac{4z'\rho + \left(z'^2 - 1\right)\left[\left(z'^2 - 1\right) + 2z'\rho + 2\right]}{2\left(2z' - \rho\left(z'^2 - 1\right)\right)z'\cos\theta + \left(z'^2 - 1\right)\left(\left(z'^2 - 1\right) + 2z'\rho\right)}\left(1 + z'^2\right)\right] \tag{22}$$

$$\theta = \operatorname{asin}\left[\frac{\sqrt{\left[2z' + \left(1 - z'^2\right)\rho\right]^2 + 8\Lambda^2\left(1 + z'^2\right)z'^2} - 2z' - \left(1 - z'^2\right)\rho}{4\Lambda z'^2}\right]$$

The blur spot size can be plotted for a desired mirror shape and aperture size.

These relationships for blur spot size can be significantly reduced by means of some simplifications and assumptions. For example, consider the special case where z'=1. For an average mirror this is somewhere near the horizontal ray. Also for most mirror shapes the blur spot is relatively independent over the mirror. By making this simplifying assumption:

$$B = \rho \frac{\sqrt{1+4\Lambda^2}-1}{2\Lambda} - \frac{\rho^2}{2-\rho}\sqrt{\frac{\sqrt{1+4\Lambda^2}-1}{2\Lambda}} \tag{23}$$

By differentiating the above expression, it can be shown that dB/dρ is positive for all typical values of ρ (i.e., ρ<1) so the maximum blur spot occurs at the outer edge of the mirror. Further, the lens aperature is typically small when compared to the focal distance from the lens to the mirror (Λ<<1). This assumption further reduces the blur spot relationship to:

$$B = \left(1 - \frac{\rho}{2-\rho}\right)\rho\,\Lambda \tag{24}$$

One final simplification is that ρ is significantly smaller than 1.0, the relation then reduces to:

$$B = \rho\,\Lambda \tag{25}$$

These surprisingly simple relationships were derived only by making reasonable assumptions about the aspect ratio of the system geometry and using a typical value for the mirror slope. This yields a lower bound for the blur spot of the axisymmetric reflector as a function of only the system's overall geometry.

Parafocal Reflector Shape

In addition to the resolution or blur spot size of the system, another important parameter is the portion of the image that can be in focus that any one time. A potentially desirable shape would allow the entire image to be in focus using a single position of the camera lens. This property could be achieved by designing the mirror shape such that the focal point of all areas of the mirror lies in a plane perpendicular to the *z*-axis. Such a mirror shape is termed a parafocal reflector. The location of the azimuthal focal point was derived earlier (Equation 15). By setting this focal point to a constant value over the surface of the mirror, a parafocal shape can be determined.

$$z_0 = z + \frac{r}{2}\frac{1+z'^2}{z'(1-\rho z')} \tag{26}$$

This relationship is a nonlinear first-order differential equation whose solution is the parafocal reflector. Solving for *z'*:

$$z' = \frac{1}{r(z-2z_0)}\left[z(z-z_0)+\sqrt{z^2(z-z_0)^2+r^2z(z-2z_0)}\right] \tag{27}$$

A closed form solution is not available. A numerical solution can be readily determined from initial conditions. Figure 16 shows the shape of a parafocal reflector with the focal plane situated 10 units from the aperture.

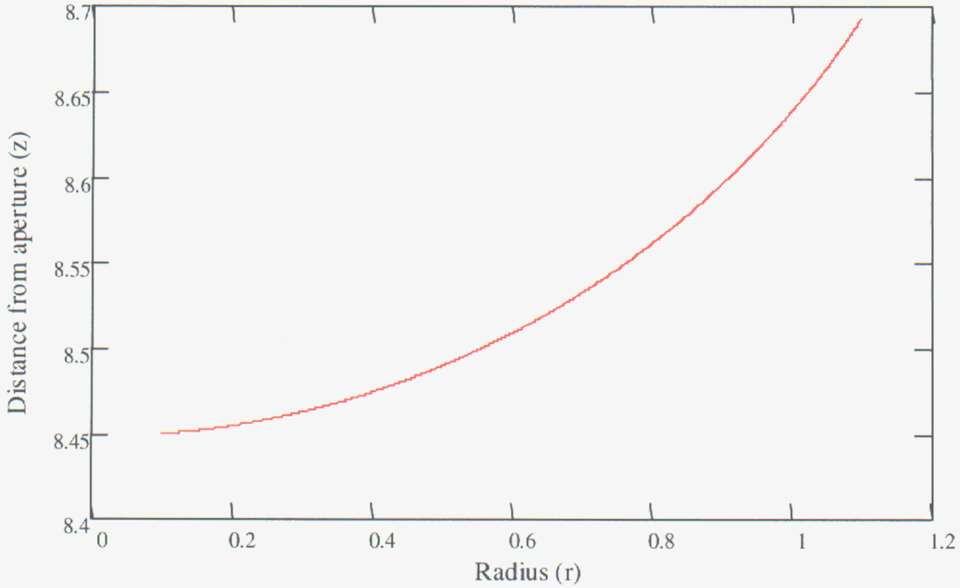

Figure 16: Shape of a parafocal reflector

From this initial analysis it does appear that a parafocal reflector may be practical.

Astigmatism Correction

All calculations to this point have ignored the aberrations introduced by the curvature along the meridian. The blur spot and parafocal calculations in that sense are lower bounds since the meridional curvature will contribute as well. One well recognized aspect of an axisymmetric reflector is astigmatism. Astigmatism means that the focal point in the meridional direction is different from that in the azimuthal direction. This property is detrimental since it greatly increases the blur spot size. This section develops relationships for determining the focal point in the meridional direction and examines the possibility of using an appropriate reflector shape to correct for astigmatism.

Consider the intersection of a ray reflected from some point on the mirror with that of a ray reflected from a point displaced slightly along the meridian. Figure 17 illustrates this geometry.

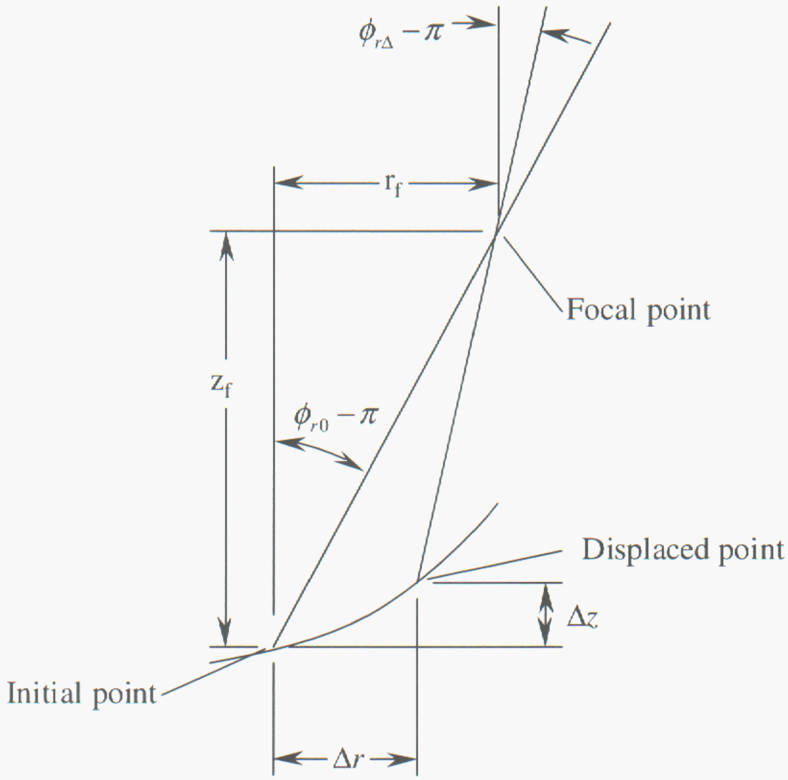

Figure 17: Geometry of the meridional focal point

The figure shows the initial point and the direction of the reflected ray ($\phi_{r0} - \pi$) as well as a point displaced by (Δr, Δz) and its reflected ray direction ($\phi_{r\Delta} - \pi$). To determine the intersection of the reflected rays, consider a sum of the r-direction components from the initial point to the focal point, on to the displaced point and back to the initial point:

$$0 = z_f \tan(\phi_{r0} - \pi) - (z_f - \Delta z)\tan(\phi_{r\Delta} - \pi) - \Delta r \tag{28}$$

Solving for z_f:

$$z_f = \frac{\Delta z \tan(\phi_{r\Delta} - \pi) - \Delta r}{\tan(\phi_{r\Delta} - \pi) - \tan(\phi_{r0} - \pi)} \tag{29}$$

The value of $\tan(\phi_{r0} - \pi)$ was determined from the trigonometric identities above. The value of the reflection angle at the displaced point can be derived by using a differential displacement from the initial point:

$$\phi_{r\Delta} = \phi_{r0} + \Delta r \frac{d}{dr}\phi_r = \phi_{r0} + \Delta r \frac{d}{dr}\left(2\phi_n - \phi + \pi\right) = \phi_{r0} + 2\Delta r \frac{d}{dr}\phi_n \tag{30}$$

by the definition of ϕ_n:

$$\frac{d}{dr}\phi_n = \frac{-1}{1+z'^2}\frac{d}{dr}z' = \frac{-z''}{1+z'^2} \tag{31}$$

Then:

$$\phi_{r\Delta} = \phi_{r0} - \frac{2\Delta r z''}{1+z'^2} \tag{32}$$

For small Δr:

$$\begin{aligned}
\tan(\phi_{r\Delta} - \pi) &= \tan(\phi_{r0} - \pi) - \frac{2\Delta r z''}{1+z'^2}\frac{\rho}{\sqrt{1+\rho^2}} \\
\tan(\phi_{r\Delta} - \pi) &= \tan(\phi_{r0} - \pi) - \frac{2\Delta r z''}{1+z'^2}\left(1 + \tan(\phi_{r0} - \pi)^2\right) \\
\tan(\phi_{r\Delta} - \pi) &= \rho - \frac{2\Delta r z''}{1+z'^2}\left(1+\rho^2\right)
\end{aligned} \tag{33}$$

Substituting Equation 33 into 29 and taking the limit as $\Delta r \to 0$ results in:

$$z_f = \frac{\left(1+z'^2\right)\left(1-z'\rho\right)}{2z''\left(1+\rho^2\right)} \tag{34}$$

As defined here z_f is the distance from the reflection point to the focal point. The height of the reflection point must be added to give the z coordinate of the meridional focal point.

$$z_0 = \frac{\left(1+z'^2\right)\left(1-z'\rho\right)}{2z''\left(1+\rho^2\right)} + z \tag{35}$$

to correct for astigmatism in the reflector this focal point can be set equal to the azimuthal focal point of Equation 15 resulting in:

$$z''=z'\frac{(z'r-z)^2}{r(z^2+r^2)} \tag{36}$$

This is the governing differential equation for an axisymmetric mirror with astigmatism correction. Since it is a second order differential equation, it does have an additional degree of freedom in the solution, being the specification of the initial value of the first derivative. No useful set of initial parameters has been discovered to produce a practical mirror. Although not conclusive, it appears that an astigmatism corrected reflector may not be practical.

Analytical Investigation Summary

Three potential optimizations of an axisymmetric reflector, resolution, parafocal behavior, and stigmatism, have been addressed here. It appears that practical reflector shapes exist that can achieve some of these optimizations. This freedom is predicated by the significant advances in real-time graphics processing that allow complex image transforms to be employed providing this freedom in shape selection. Other areas of optimization exist which have not been addressed here such as minimizing the overall blur spot for both azimuthal and meridional directions.

It appears that significant room for improvement exists in the development of an axisymmetric reflector. The optimizations present here and perhaps others should be seriously considered in producing a design of a high-performance 360 degree imaging system.

Summary and Conclusions

This work focused on demonstrating the feasibility of a new optical configuration applicable to a MEMS scale high-performance imaging system. A large-scale proof of concept system was constructed which provided wide pan and tilt ranges with only small motions of a single mirror. The system produced high-resolution images from a portion of a convex mirror. Texture mapping software was developed to correct the image distortion produced by a variety of convex mirror surfaces. Analytical methods for determining blur spot size and tools for optimizing mirror shape based on selected criteria were also developed.

The results of this effort were promising and provide a good first step towards the goal of a small-scale high-performance optical system. The results indicate further investigation is warranted. The tools developed here should be useful in pursuing that end.

References

[1] Nayar, S. K., “Omnidirectional Vision”, Eighth International Symposium of Robotics Research, Hayama, Japan, October 1997.

[2] Vision Technologies Inc., Infinity Focus Lens, Rogers , AR.

[3] Leger, Chris, “Determining the Viability of Parabolic Mirrors for Micro Machines”, poster session, Sixth Annual Student Internship Program Symposium, August 2001.

[4] Gottlieb, E., McDonald, M., Oppel, F., “Umbra’s High Level Architecture (HLA) Interface”, April 2002, Sandia Internal Report, SAND2002-0675.

Distribution

1	MS1002	G. R. Langhiem, 15200
1	MS1205	D. Nokes, 5900
1	MS1002	M. Swinson, 15203
1	MS0970	S. Gutierrez, 5700
1	MS1003	K. M. Jensen, 15212
1	MS1003	R. D. Robinett, III, 15211
5	MS1003	C. W. Wilson, 15212
5	MS1003	B. L. Spletzer, 15211
1	MS1003	C. L. Leger, 15212
5	MS1003	ISRC Technical Library, 15200

1	MS0188	LDRD Office, Attn: Donna Chavez, 1030
1	MS9018	Central Files, 8945-1
2	MS0899	Technical Library, 9616
1	MS0612	Review & Approval Desk, 9612

Intentionally Left Blank